On the Accuracy of Topographic Residuals Retrieved by MTInSAR

Yanan Du, Lei Zhang, Guangcai Feng, Zhong Lu, and Qian Sun

***Abstract*— Topographic residuals in differential interferometric synthetic aperture radar (InSAR) measurements are mainly caused by inaccurate external digital elevation model (DEM). Accurate separation of the phase component contributed by topographic residuals plays an important role in the retrieval of deformation time series from InSAR observations. Even though the residuals can be modeled and estimated in the framework of multitemporal SAR interferometry (MTInSAR), it is not clear what an optimal processing strategy is and how accurate the estimation can reach. We analyze here the factors that affect the accuracy of the retrieved DEM residuals by applying four commonly used MTInSAR methods in a series of simulated scenarios. The results indicate that besides the quality of interferometric observations, the thresholds of spatial and temporal baselines, the diversity of spatial baseline lengths, the connectivity of interferogram network, and improper deformation model also fluctuate the accuracy of the retrieved topographic residuals. According to these affecting factors, this paper sheds light on an optimal approach to reliably retrieve accurate topographic residuals under MTInSAR framework.**

***Index Terms*— Digital elevation model (DEM) error estimation, multitemporal synthetic aperture radar interferometry (MTInSAR), topographic residuals.**

I. Introduction

BY VIRTUE of its high precision and wide coverage, differential interferometric synthetic aperture radar (InSAR) technology has been widely used in monitoring land deformation caused by either natural or anthropogenic processes, such as volcanic eruption, earthquakes, landslides, and ground subsidence [1]–[7]. However, the interpretation and analysis of DInSAR measurements are affected by spatial–temporal decorrelation, atmospheric artifacts, orbit inaccuracy, topographic phase residuals, and phase unwrapping errors. To minimize or eliminate these influences, multitemporal InSAR (MTInSAR) methods involving analyzing large sets of SAR images have been proposed, such as the small baseline subset (SBAS), permanent scatterer (PS), and hybrid SBAS/PS techniques [8]–[15]. Some techniques work directly on the wrapped phases of high-quality scatterers [8]–[11], while some can get deformation from unwrapped phases at selected pixels in interferograms with moderate spatial and temporal baselines [12]–[14]. For all MTInSAR techniques aiming to retrieve deformation signal, the phase component raised by inaccurate external digital elevation model (DEM), i.e., topographic residuals, should be estimated and removed from either wrapped or unwrapped phase observations [8]–[15]. The topographic residual that is a baseline-dependent component and usually modeled as a parameter in MTInSAR can lead to phase discontinuities and even coherence loss in the wrapped differential interferograms, resulting in a failure of phase unwrapping. In the scenarios of geohazard (e.g., landslides) mapping, inaccurately estimated topographic residuals can be mistaken as geohazard induced deformation signal, and likely distort the interpretation of its spatial–temporal behavior. Accurate estimation of topographic residuals can not only provide refined height product from SAR data but also improve the success rate of phase unwrapping and the quality of MTInSAR derived deformation time series [16], [17].

However, current MTInSAR techniques cannot promise an accurate estimation of the topographic residuals. For example, the conventional SBAS based on interferograms with small spatial and temporal baselines to reduce decorrelation cannot well estimate DEM error when the perpendicular baseline is time dependent, such as the case depicted in [18] and [19]. In addition, the DEM error estimated by conventional SBAS method is sensitive to the interferograms network, which is relevant to the spatial–temporal baseline thresholds among SAR acquisitions [20]. Moreover, improper deformation model can also bias the estimation of topographic residuals from SAR data [21].

We dedicate here to explore the factors having influence on the estimation of topographic residuals. By analyzing the performance of four popularly used MTInSAR models under a large amount of simulated scenarios, we conclude that the accuracy of InSAR derived topographic residuals is closely related to the factors such as the baseline thresholds, interferogram quality, interferogram network subset, and deformation models. This paper not only raises the awareness of shortcomings associated with existing MTInSAR models, but also

Manuscript received April 12, 2016; revised August 17, 2016; accepted October 10, 2016. Date of publication November 4, 2016; date of current version December 29, 2016. This work was supported in part by the Research Grants Council of Hong Kong under Grant PolyU5381/13E and Grant PolyU152214/14E, in part by the National Natural Science Foundation of China under Grant 41304011 and Grant 41574005, and in part by the Public Project of State Bureau of Surveying and Mapping. *(Corresponding author: Lei Zhang.)*

Y. Du and G. Feng are with the School of Geosciences and Info-Physics, Central South University, 410083 Changsha, China (e-mail: yndu_csu@csu.edu.cn; fredgps@gmail.com).

L. Zhang is with the Department of Land Surveying and Geo-Informatics, The Hong Kong Polytechnic University, Hong Kong (e-mail: lslzhang@polyu.edu.hk).

Z. Lu is with the Roy M. Huffington Department of Earth Sciences, Southern Methodist University, Dallas, TX 75275, USA (e-mail: zhonglu@mail.smu.edu).

Q. Sun is with the College of Resources and Environmental Science, Hunan Normal University, 410006 Changsha, China (e-mail: sunqian200241@aliyun.com).

Color versions of one or more of the figures in this paper are available online at http://ieeexplore.ieee.org.

Digital Object Identifier 10.1109/TGRS.2016.2618942

sheds light on the possible ways to reliably retrieve accurate topographic residuals under MTInSAR framework. We start with a brief description of how the topographic residuals are modeled under MTInSAR framework. Then we analyze the accuracy of these models to identify the relationship between topographic residuals and influence factors through a series of validation experiments. Finally, the results and conclusions are obtained to give guidance for accurate DEM error estimation.

II. Models for Topographic Residual Estimation in MTInSAR

Given $N+1$ SAR images, N interferograms will be generated under single-master MTInSAR framework and M ($M \geq N$) under multiple-master MTInSAR framework. Observations for single-master MTInSAR [8]–[11] are usually the wrapped phases at PSs, while both wrapped and unwrapped phases can be used as observations for the multiple-master MTInSAR [7], [12], [13], [15]–[20]. The differential interferometric phase $\delta\phi^{t_A,t_B}$ between two SAR acquisitions at time t_A and t_B can be expressed as

$$\begin{aligned}\delta\phi^{t_A,t_B} &= W\{\delta\varphi^{t_A,t_B}\} \\ &= W\left\{\delta\varphi_{\text{def}}^{t_A,t_B}+\delta\varphi_{\text{topo}}^{t_A,t_B}+\delta\varphi_{\text{orb}}^{t_A,t_B}+\delta\varphi_{\text{aps}}^{t_A,t_B}+\delta\varphi_{noi}^{t_A,t_B}\right\} \\ &= W\left\{-\frac{4\pi}{\lambda}\left(d^{t_A}-d^{t_B}\right)-\frac{4\pi\, B_{\perp}^{t_A,t_B}}{\lambda R sin\theta}\Delta z+\delta\varphi_{\text{orb}}^{t_A,t_B}\right. \\ &\qquad \left.+\delta\varphi_{\text{aps}}^{t_A,t_B}+\delta\varphi_{n}^{t_A,t_B}\right\} \end{aligned} \tag{1}$$

where $\delta\varphi^{t_A,t_B}$ is the unwrapped phase and $W\{\cdot\}$ is the wrap operator. $\delta\varphi_{\text{def}}^{t_A,t_B}$, $\delta\varphi_{\text{topo}}^{t_A,t_B}$, $\delta\varphi_{\text{orb}}^{t_A,t_B}$, $\delta\varphi_{\text{aps}}^{t_A,t_B}$, and $\delta\varphi_{n}^{t_A,t_B}$ represent the phase components contributed by the deformation along the line of sight direction, topographic residual, orbit error, atmospheric delay, and noise, respectively. d^{t_A} and d^{t_B} represent the deformation at t_A and t_B. $B_{\perp}^{t_A,t_B}$ is the perpendicular baseline, and Δz is the DEM error. R, θ, and λ represent the distance between satellite and ground target, incidence angle, and wavelength, respectively.

A. Permanent Scatterer InSAR—Model 1

PSInSAR, a typical single-master MTInSAR technique, was proposed in [8] and [9], aiming at retrieving deformation from persistent scatterers (PSs) at a full resolution scale. The DEM error and mean velocity of deformation are estimated with a simple periodogram by searching a predefined 2-D solution space [8]

$$\underset{\Delta z,v}{\text{argmax}}\left\{|\gamma|=\frac{1}{N}\sum\nolimits_{n=1}^{N}e^{j\delta\phi^{n}}\cdot e^{-j\left(\frac{4\pi\cdot\Delta z}{\lambda R sin\theta}B_{\perp}^{n}+\frac{4\pi}{\lambda}t_n\cdot v\right)}\right\} \tag{2}$$

where $\delta\phi^{n}$ and $B_{\perp}^{n}$ represent the wrapped interferometric phase and perpendicular baseline of nth interferograms. Provided that the predefined model is consistent with the real ground deformation, the accuracy of the estimated DEM error is generally high [22], [23].

B. Conventional SBAS—Model 2

Assuming that M interferograms are obtained from $N+1$ SAR images with a spatial–temporal baseline thresholds, the M differential interferograms are unwrapped successfully and the residue orbit phases are removed with a polynomial. The unwrapped differential phase $\delta\varphi$ of any pixel can be expressed as follows [13], and named the "original unwrapped phase" hereafter:

$$\delta\varphi=\delta\varphi_{\text{def}}+\delta\varphi_{\text{topo}}. \tag{3}$$

In (3), deformation component $\delta\varphi_{\text{def}}$ can be modeled using analytic functions such as a third-order polynomial with three unknown parameters, i.e., the mean velocity $\bar{v}$, the mean acceleration $\bar{a}$, and the mean acceleration rate $\Delta\bar{a}$ at time t_i with an interval of $\Delta\mathbf{t_i}$ with respect to the reference acquisition time t_0

$$\delta\varphi_{\text{def}}^{t_i}=\bar{v}\,\Delta t_i+\frac{1}{2}\bar{a}\,\Delta t_i^2+\frac{1}{6}\Delta\bar{a}\,\Delta t_i^3. \tag{4}$$

And the observation equation of M differential interferograms can be obtained by combining (1), (3), and (4)

$$\delta\varphi=[BH,c]p \tag{5}$$

where B is an $M\times N$ matrix created in the following way. If the kth interferogram constructs between the ith and jth SAR images ($i<j$), then the value between column i and $j-1$ of B equals the time interval of adjacent SAR images. p is the vector of unknown parameters equal to $[v,\bar{a},\Delta\bar{a},\Delta z]^T$, and c is the parameter of residue topographic phase equal to $[(4\pi/\lambda R\sin\theta)B_{\perp}^{1}(4\pi/\lambda R\sin\theta)B_{\perp}^{2}\ldots(4\pi/\lambda R\sin\theta)B_{\perp}^{M}]^T$. H is an $N\times 3$ matrix as follows:

$$H=\begin{bmatrix}1 & \Delta t_1/2 & \Delta t_1^2/6\\ 1 & (\Delta t_2+\Delta t_1)/2 & \Delta t_2^3-\Delta t_1^3/(6t_2-6t_1)\\ \vdots & \vdots & \vdots\\ 1 & (\Delta t_N+\Delta t_{N-1})/2 & \Delta t_N^3-\Delta t_{N-1}^3/(6t_N-6t_{N-1})\end{bmatrix}. \tag{6}$$

It is worth noting that the unknown parameters can be further simplified to the mean velocity and the DEM error, which have been adopted in many applications [24]. We can obtain the DEM error with a least squares method by treating atmosphere and decorrelation artifacts as stochastic noises [13]. However, the accuracy of the estimated DEM error is sensitive to baseline configuration of the selected interferograms and inaccurately estimated DEM error can further affect the retrieval of deformation time series [20]. Meanwhile, according to [18], the estimation is also not accurate when the baseline history has an intense time-dependent relationship.

C. Samsonov's Model—Model 3

A model simultaneously estimating the DEM error and velocity time series was proposed in [18] and [19] to deal with the case that perpendicular baselines of ALOS/PALSAR interferograms are time dependent. Similar to conventional SBAS, this model is also based on the original unwrapped phase $\delta\varphi$ of M interferograms, but with different unknown parameters, which includes N velocities between adjacent

TABLE I
COMPARISON BETWEEN DIFFERENT MTINSAR MODELS

Function models	Unknown parameters (X)	Observations (B)	solution	Design matrix (A)
1、PSInSAR	$\bar{v}, \Delta z$	$W\{\delta\varphi_i\}, i = 1,2,\ldots,N$	periodogram	-
2、traditonal SBAS	$\bar{v}, \bar{a}, \Delta\bar{a}, \Delta z$	$\delta\varphi_i, i = 1,2,\ldots,M$	LS	M × 4
3、Samsnovo's	$[v_1, v_2, \ldots, v_N, \Delta z]^T$	$\delta\varphi_i, i = 1,2,\ldots,M$	SVD	M × (N + 1)
4、Fahatti's	$\bar{v}, \bar{a}, \Delta\bar{a}, \Delta z$	$[v_1, v_2, \ldots, v_N]^T$	SVD,LS	M × N

acquisitions, i.e., V to be jointly estimated together with DEM error. Accordingly, the design matrix is also different, which is described as

$$\delta\varphi = [Bc] \cdot [V\,\Delta z]^T \tag{7}$$

where V is the velocity vector to be estimated in a form of $[v_1 v_2 \ldots v_N]^T$. B is an $M \times N$ matrix reflecting the phase contribution of interval velocities, and c is a vector with M elements, having the same form as (5), reflecting the contribution of topographic residuals. Both components constitute the design matrix of this model.

Unlike the least squares used in (5) of conventional SBAS, the singular value decomposition (SVD) is applied to jointly estimate DEM error and interval deformation rates. As the observation system is rank deficiency, the estimation stability of this model can be affected by the connectivity of interferogram network.

D. Fattahi's Model—Model 4

Fattahi and Amulung [20] proved that the accuracy of the estimated DEM error in conventional SBAS is sensitive to the interferogram network. To tackle this problem, they estimate the DEM error based on the velocity vector derived from the original unwrapped phases of M interferograms. First, they estimated the velocity vector $V = [v_1, v_2, \ldots, v_N]^T$ from the original unwrapped phases with SVD and then estimated DEM error of each coherent pixel with the following model:

$$V = A \cdot X + n \tag{8}$$

where we have (9) and (10), shown at the bottom of the page.

This linear equation can be solved by least squares thanks to the redundant observations. Since the model can estimate DEM error from phase components in successive time intervals, it can well reduce the sensitivity of DEM error estimation in the interferogram network. In other words, no matter how the selected interferogams with short baselines are connected, the estimation of DEM error appears to be stable. However, the performance of this model is also affected by the connectivity of interferogram network and the discrepancy between the deformation model used and the real deformation, which will be analyzed in Section III.

III. ACCURACY ANALYSIS

A. Baseline Thresholds

The function models of MTInSAR, except PSInSAR methods in [8] and [9], can be expressed in a general form as follows:

$$B = A \cdot X + n \tag{11}$$

where the design matrix and unknown parameters vary with different models. For example, there are four unknown parameters in conventional SBAS (Model 2) and $N + 1$ in Samsnovo's model (Model 3). Fahatti's model (Model 4) has two sets of unknown parameters. One is the velocity vector with N unknowns, and the other set is the same as those used in Model 2. Table I summarizes the key features of the four MTInSAR models that will be used for retrieval of topographic residuals in the following section.

It is worth noting that we can obtain the result of Models 2 and 4 by least squares if the design matrix is not rank deficiency, and can obtain the unknown parameters X and the corresponding covariance matrix $Q_{\hat{X}\hat{X}}$

$$\hat{X} = (A^T P A)^{-1} A^T P B \tag{12}$$

$$Q_{\hat{X}\hat{X}} = (A^T P A)^{-1} \tag{13}$$

where P is the weight matrix of observations. The covariance matrix of Model 4 should be estimated with error

$$A = \begin{bmatrix} 1 & \Delta t_1/2 & \Delta t_1^2/6 & \frac{4\pi}{\lambda \mathrm{R}\sin\theta}\frac{B_\perp^1 - B_\perp^0}{t_1 - t_0} \\ 1 & (\Delta t_2 + \Delta t_1)/2 & \Delta t_2^3 - \Delta t_1^3/(6t_2 - 6t_1) & \frac{4\pi}{\lambda \mathrm{R}\sin\theta}\frac{B_\perp^2 - B_\perp^1}{t_2 - t_1} \\ \vdots & \vdots & \ddots & \vdots \\ 1 & (\Delta t_N + \Delta t_{N-1})/2 & \Delta t_N^3 - \Delta t_{N-1}^3/(6t_N - 6t_{N-1}) & \frac{4\pi}{\lambda \mathrm{R}\sin\theta}\frac{B_\perp^N - B_\perp^{N-1}}{t_N - t_{N-1}} \end{bmatrix} \tag{9}$$

$$X = [\bar{v}\,\bar{a}\,\Delta\bar{a}\,\Delta z]^T. \tag{10}$$

propagation, because of the changing observations from the original unwrapped phase to velocity vector. In addition, the variance–covariance matrix of unknown parameters of Model 3 whose design matrix (A) is rank deficiency can be determined according to its generalized inverse of A.

It is clear that the design matrix A determined by the thresholds of baselines used for selecting interferograms is a main factor in $Q_{\hat{X}\hat{X}}$ and can affect the accuracy of the unknowns. The design matrix corresponding to small baseline thresholds will result in a poor or instable estimation of the unknown parameters [25]. The relationship between the accuracy of the estimated DEM error and the thresholds and variation of baselines will be thoroughly analyzed via a large set of synthetic tests.

B. Connectivity of Interferogram Network

As described above, different baseline thresholds can lead to different design matrices. Interferogram subsets can also be possibly induced due to small thresholds or coarse temporal density of SAR images. The subsets can make the design matrix rank deficiency, and therefore parameter estimation has to depend on extra constraints. Minimum norm constraint behind SVD that has been widely used in multiple-master MTInSAR methods cannot guarantee a reliable estimation of parameters (e.g., the topographic error and deformation), especially in the case that there is notable fluctuation among parameters.

C. Deformation Assumptions

Linear and cubic deformation assumptions are widely used in MTInSAR models [13], [15], [27]. However, the discrepancy between the real deformation pattern of a study area and the assumed model hinders us to get an accurate estimation of DEM error. Moreover, the inaccurately estimated DEM error will further induce contamination to the deformation time series estimation and the elimination of atmospheric phase.

IV. Synthetic Tests and Results

Abundant tests have been conducted in order to identify the relationship between the accuracy of MTInSAR derived topographic residuals and the factors described in Section III. We have simulated 33 interferograms where temporal and perpendicular baselines of an Envisat/ASAR Track 175 over Pearl River Delta, China, are used. The baseline distribution is shown in Fig. 1(a). A total of 1500 pixels are sampled from a real deformation field to guarantee the spatial correlation of deformation. Meanwhile, three deformation models with different magnitudes, i.e., linear [Fig. 1(b)], periodic [Fig. 1(c)], and complicated [Fig. 1(d)], DEM error, atmospheric effects, and decorrelation noise are also simulated and used to generate the interferograms. As DEM error is taken as a parameter in MTInSAR techniques, essentially speaking, models used for DEM error simulation will not affect the estimation. However, to make the DEM error more realistic, we adopt here the difference between DEM retrieved from TanDEM-X [Fig. 2(a)] and SRTM DEM [Fig. 2(b)] as the "true"

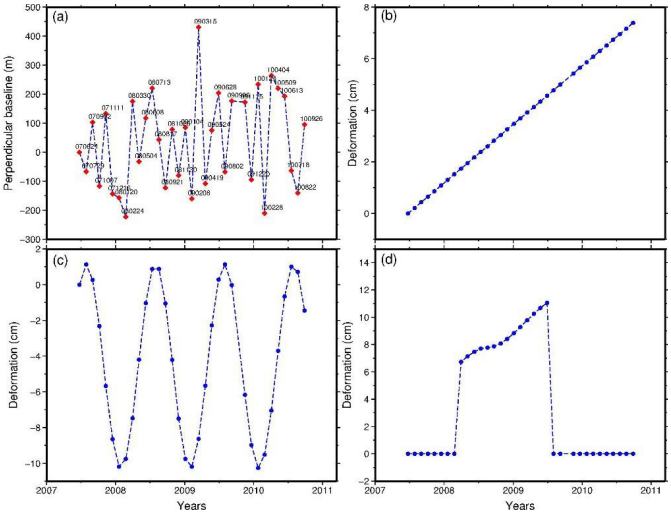

Fig. 1. (a) Distribution of spatial–temporal baselines. (b) Simulated linear deformation. (c) Simulated periodical deformation. (d) Simulated complex deformation.

value of DEM error at the selected coherent points, as shown in Fig. 2(c) and (d). To analyze the atmospheric effects, atmospheric signal is simulated with the fractal dimension that has a uniform distribution between 2.16 and 2.67 at a wavelength about 0.5–2 km [28], [29]. The atmospheric artifacts in the simulated 34 SLCs are spatially correlated, while with random magnitudes, whose maximum varies randomly with a standard deviation of 0.5, 1.5, 2.5, and 3.5 rad for analyzing the relationship between RMSE of DEM error and atmospheric artifacts. As an example, one set of artifacts having a standard deviation of 1.5 rad is shown in Fig. 3, which is used as the atmospheric phases in scenarios for analyzing the effects of other factors on the accuracy of estimated DEM error. In addition, the decorrelation noise caused by geometric, temporal, and volume is also taken into consideration based on an assumed zero-Doppler centroid frequency, resulting in a spatial- and temporal-related phase noise as follows [29], [30]:

$$\begin{aligned}\gamma^{k,m} &= \gamma_{\text{geometric}} \cdot \gamma_{\text{temporal}} = g(B_{\perp}^{k,m}, B_{\perp\text{critical}}) \\ &\quad \cdot g(T^{k,m}, T_{\text{critical}}) \\ g(x,c) &= \begin{cases} 1 - \dfrac{|x|}{c}, & \text{if } |x| < c \\ 0, & \text{otherwise} \end{cases}\end{aligned} \tag{14}$$

where k and m are two SAR images, $B_{\perp}^{k,m}$ and $T^{k,m}$ are the perpendicular and temporal baselines of interferograms, and $B_{\perp\text{critical}}$ and T_{critical} are the critical spatial and temporal baselines of interferograms. The critical baseline is a function of wavelength, incidence angle, and topographic slope derived from DEM [29], [30], and the critical temporal baseline is set to five years considering the stability of man-made targets, such as buildings and streets, in this paper [28]. It is worth noting that the orbit errors are assumed to be well removed from the interferometric phases, which can be achieved using the model proposed in [1], [7], and [31] in real cases. We can then get a set of simulated wrapped and unwrapped interferograms with different spatial and temporal baseline thresholds.

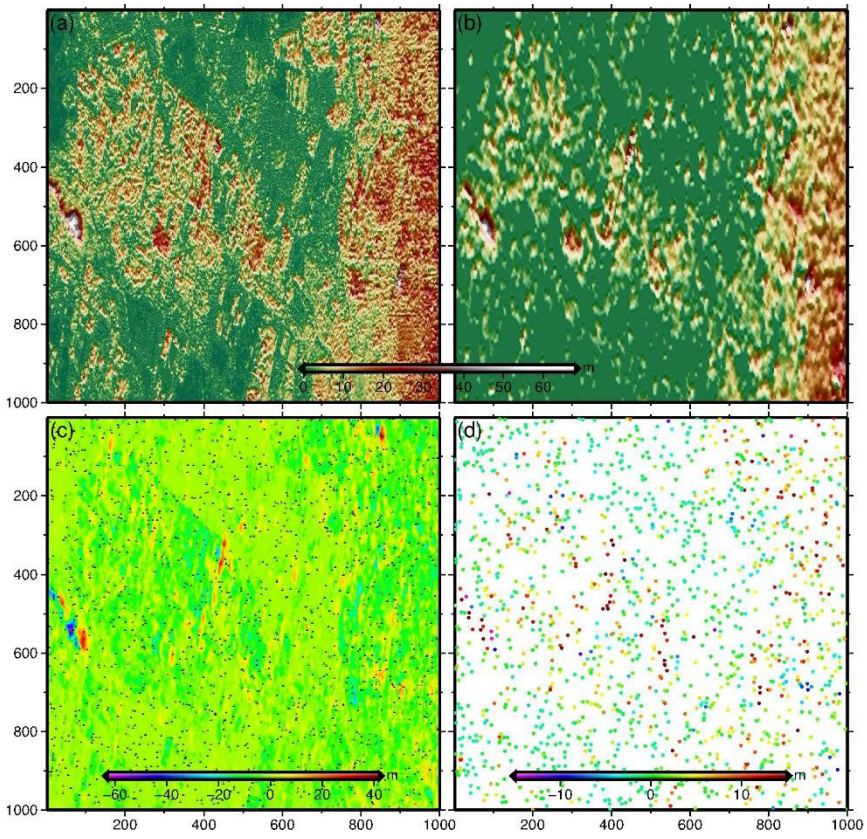

Fig. 2. (c) and (d) DEM error map derived from the difference between (a) TanDEM-X and (b) SRTM.

To tackle the relationship between the accuracy of the estimated DEM error and the factors depicted above, we independently analyze the impact of each factor on the popular MTInSAR models introduced in Section II. For example, we will fix the baseline threshold and deformation pattern when we analyze the influence of network connectivity on DEM error estimation. The accuracies of the estimated DEM error and time series deformation for four adopted models are quantified by the root-mean-square error (RMSE) between the estimated and the simulated "true" DEM

$$\mathrm{rmse}(Z) = \sqrt{\sum_{i=1}^{\mathrm{Num}} (Z_{\mathrm{est}} - Z_{\mathrm{true}})^2 / \mathrm{Num}} \tag{15}$$

$$\mathrm{rmse}(d) = \sqrt{\sum_{i=1}^{N+1} (d_{\mathrm{est}}(t_i) - d_{\mathrm{true}}(t_i))^2 / (N+1)} \tag{16}$$

where Z_{true} and d_{true} (t_i) are the "true" values of DEM error and displacement, Z_{est} and $d_{\mathrm{est}}(t_i)$ are the estimated values of two types of unknowns, and Num and $N+1$ are the number of simulated points and SLCs, respectively.

A. Relationship Between DEM Error and Baseline Thresholds

To identify the relationship between the RMSE of the estimated DEM error and baseline thresholds, we add phase components related to linear deformation, DEM error, atmospheric artifacts whose maximum variation of amplitude is set randomly with a standard variation of 1.5 rad, and baseline related noise to the simulated interferograms. It should be noted that to avoid the affection of other factors, in this simulation scenario, there are no deformation model error and interferogram subset. First, we generate a large amount of different sets of interferograms through changing the thresholds of spatial baseline from 120 to 350 m with an interval of 10 m and temporal baseline from 6× cycle days to 675 days with an interval of 2× cycle days, which serve as basic observations for the MTInSAR models. The cycle equals the satellite repeating period, which is 35 days for Envisat/ASAR. As the single-master-based PSI technique (i.e., Model 1) is not affected by baseline threshold, we ignore the evaluation of this model here. We first estimate the DEM error with Model 2, and Fig. 4(a) reflects the relationship between RMSE of the estimated DEM error and baseline thresholds. We can find that the RMSE of DEM error decreases with the rise of baseline thresholds, especially the spatial baseline. To determine the specific relationship, we calculate the mean values of each column and row and plot them in a 2-D map shown in Fig. 4(b). We can see that the RMSE of DEM error decreases with the rise in the perpendicular baseline threshold, while it stays steady with the increase in temporal baseline threshold. This indicates that the RMSE of DEM error is more sensitive to perpendicular baseline threshold and the regression model is also plotted in Fig. 4(d). Obviously, the RMSE of DEM error in SBAS InSAR (i.e., Model 2) decreases with

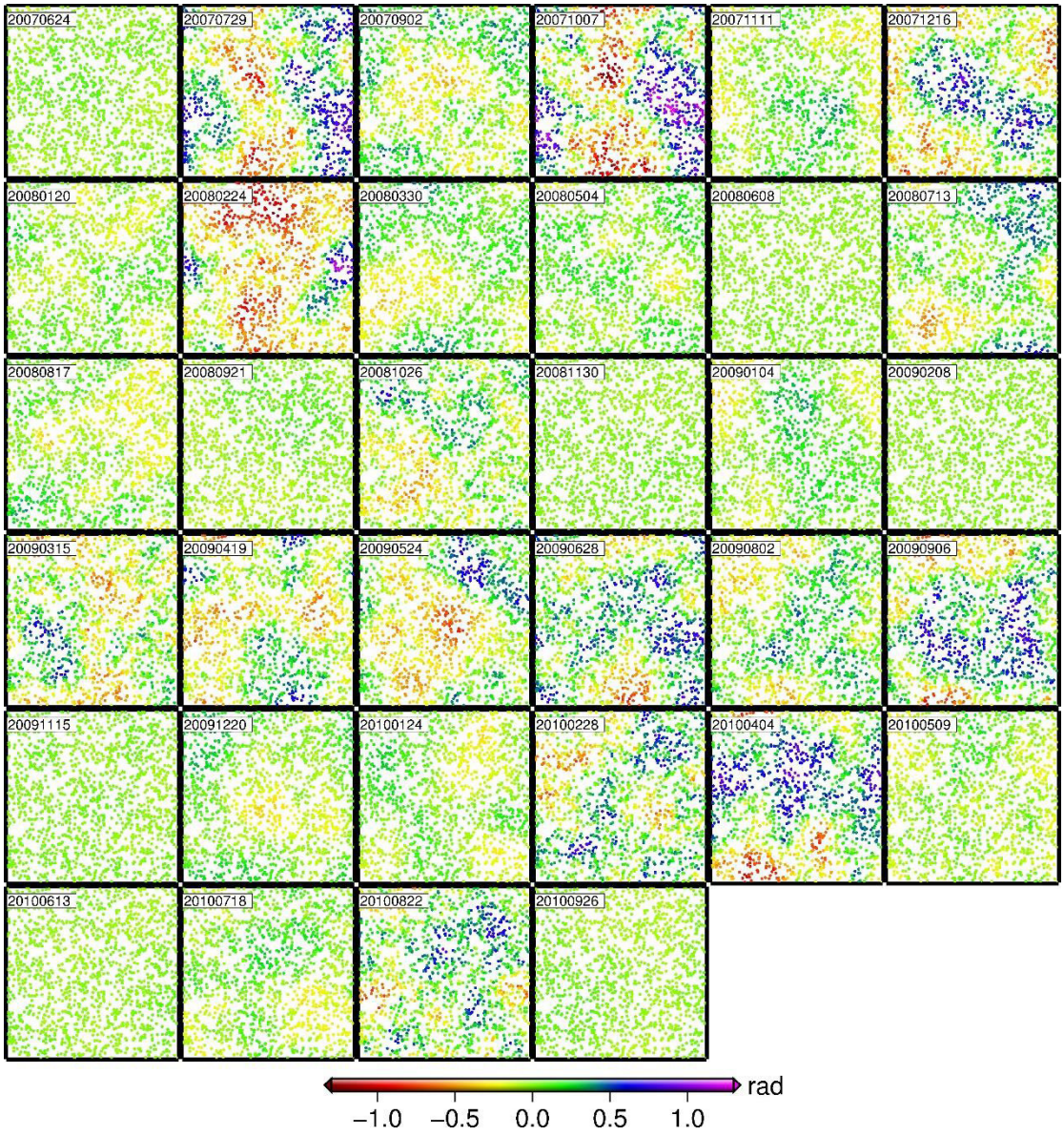

Fig. 3. Simulated atmospheric signals whose maximum variation is set randomly with a standard deviation of 1.5 rad.

the increasing perpendicular baseline threshold and it keeps steady when the baseline threshold is large enough. Moreover, we analyze the distribution of perpendicular baseline depicted by the standard deviation of baseline and plot it in Fig. 4(c), which indicates that the RMSE of DEM error decreases with the increase in perpendicular baseline diversity.

In addition, we also generate the results of Models 3 and 4. Fig. 5(a) and (b) presents the relationship between RMSE of DEM error and perpendicular baseline threshold. We can find that the RMSE of DEM error estimated by these two models [Fig. 5(a) and (b)] is almost the same ranging from 0.5 to 1.3 m and has a rather weak correlation with baseline threshold used. In other words, Models 3 and 4 are not sensitive to how the image pairs are selected. However, four obvious jumps in Fig. 5(a) and (b) are observed despite the fact that the RMSE of DEM error is approximate. For example, the first jump appears when a SAR image (March 15, 2009) is deleted due to the limitation of spatial–temporal baseline thresholds (220 m and 220 days). The following three jumps are also caused by the removal of the SAR acquisitions.

B. Relationship Between DEM Error Estimation and Interferogram Quality

We further investigate the relationship between the RMSE of the estimated DEM error and the quality of differential phase (atmospheric delay) where other factors such as deformation model, baseline thresholds (spatial and temporal baseline threshold equal to 150 m and 400 days, respectively), and interferogram connectivity have been fixed. In order to determine the atmospheric influence on DEM error, linear deformation, baseline-related noise, and four sets of atmospheric signals whose maximum amplitudes vary randomly with a standard deviation of 0.5, 1.5, 2.5, and 3.5 rad are added to the simulated interferograms. As shown in Table II, the RMSE of DEM error increases with the increasing atmosphere levels for all models. As expected, the RMSE of the DEM error

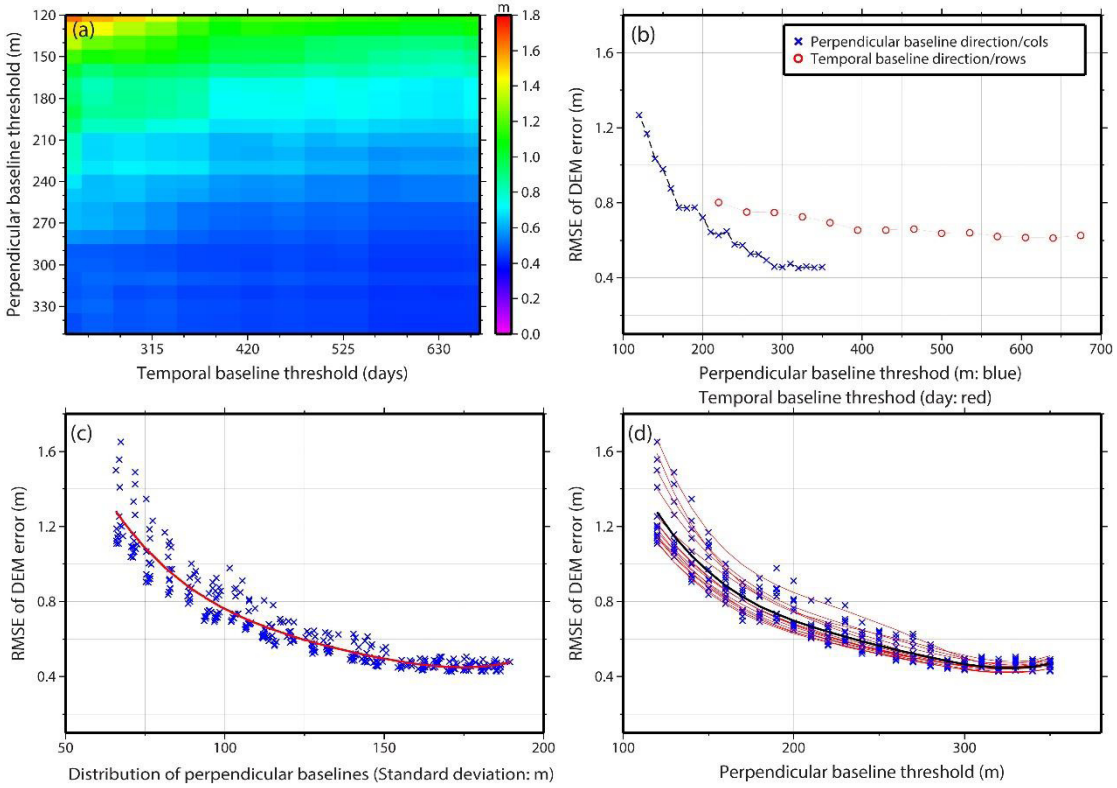

Fig. 4. (a) Relationship between RMSE of the estimated DEM error and baseline thresholds in MTInSAR methods. (b) Sensitivity of DEM error to the baseline thresholds. The horizontal axis represents the mean value of DEM error RMSE of (a) in each row (perpendicular baseline direction) or column (temporal baseline direction). The blue asterisk and red circle lines represent the sensitivity to perpendicular baseline threshold and temporal baseline threshold, respectively. (c) Relationship between RMSE of DEM error and distribution of perpendicular baseline depicted by the standard deviation of baseline. (d) Relationship between RMSE of DEM error and perpendicular baseline threshold. The red solid lines represent the regression of each column of (a), and the black solid line represents the regression of all pixels of (a).

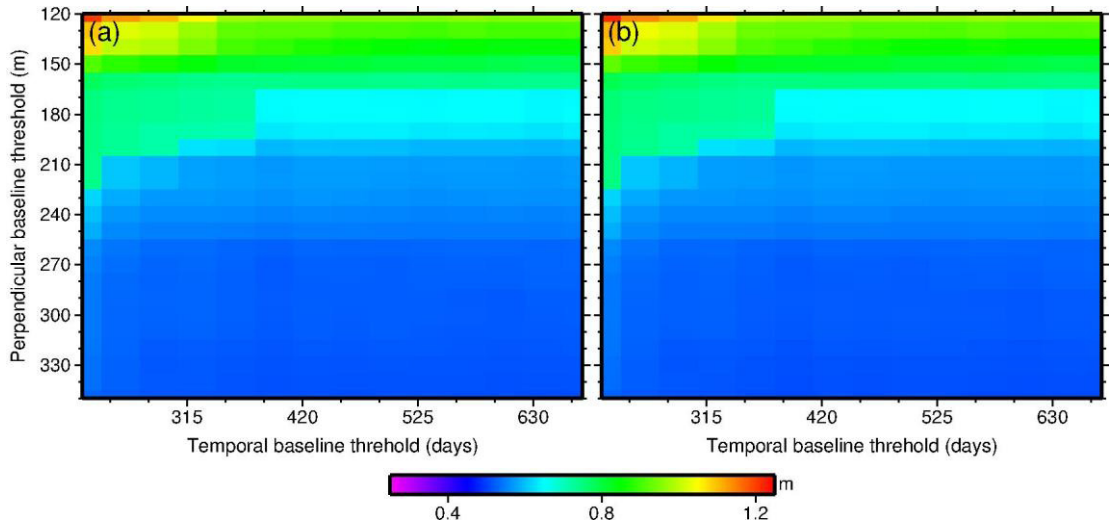

Fig. 5. Relationship between RMSE of DEM error and baseline thresholds of Models (a) 3 and (b) 4.

estimated by Models 3 and 4 is lower due to better structures of design matrix that are more sensitive to the DEM error.

C. Relationship Between DEM Error Estimation and Interferogram Subsets

As described in Section III-B, accurate estimation of DEM error by Models 3 and 4 cannot be guaranteed when subsets exist. In the synthetic test, we select image pairs with a spatial baseline threshold of 100 m and a temporal baseline threshold of 400 days and generate a network of interferograms shown in Fig. 6(a). Linear deformation, DEM error, atmospheric signals, and baseline-related noise phase are added to these selected pairs. The estimated topographic residuals and histograms of the related estimation errors for Models 2–4 are

TABLE II
STATISTICAL RESULTS OF RMSE OF DEM ERROR WITH DIFFERENT LEVELS OF ATMOSPHERE

	MaxAPS=0.5rad (m)	MaxAPS=1.5rad (m)	MaxAPS=2.5rad (m)	MaxAPS=3.5rad (m)
Model 1	0.93	0.99	1.16	2.11
Model 2	0.48	1.03	1.45	1.61
Model 3	0.59	0.81	0.99	1.38
Model 4	0.60	0.82	1.01	1.38

MaxAPS: the standard deviation of the maximum variation for atmospheric signals during the acquisitions.

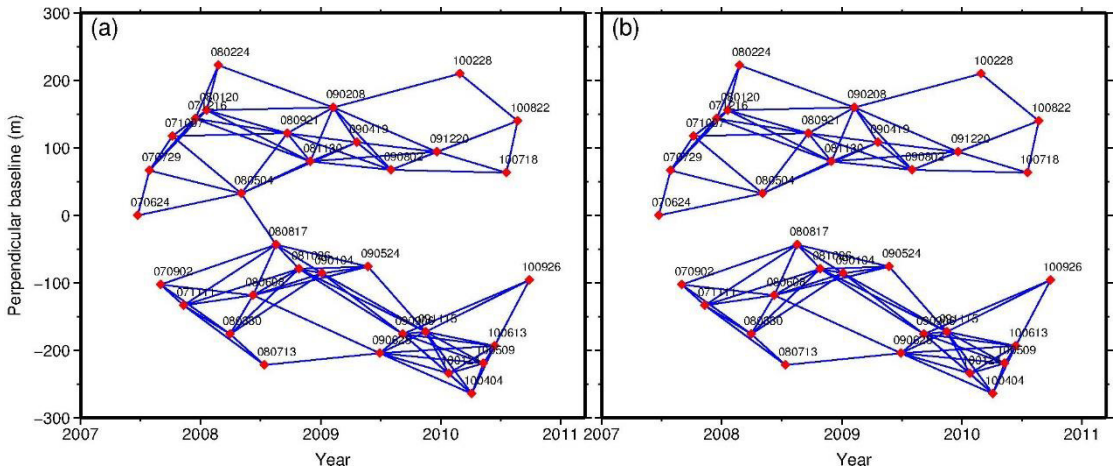

Fig. 6. (a) Distribution of selected pairs when spatial baseline threshold equals 100 m and temporal baseline threshold equals 400 days. (b) Distribution of the selected pairs with a manual deletion.

calculated and plotted in Figs. 7(a)–(c) and 8(a)–(c), respectively. The calculated RMSEs of DEM estimation error are 1.51, 1.32, and 1.33 m for these three models, respectively. Then, we delete a selected pair manually to get a network with a subset [see Fig. 6(b)]. The results for the three selected models are shown in Figs. 7(d)–(f) and 8(d)–(f), indicating that Model 2 has lower sensitivity to subset than the other two models with an RMSE of 1.57 m, which is similar to the results derived from network without subset. However, the accuracy of the estimated DEM error drops down notably for the latter two models, especially for Model 4, with the RMSE increasing from 1.33 to 4.61 m [see Fig. 7(c) and (f)]. It can be concluded that the connectivity of the network is a significant factor affecting DEM error accuracy in multimaster-based MTInSAR models. Since Model 1 naturally takes a complete network of interfergorams (i.e., no subsets) as observation, it is not necessary to evaluate the effect of subsets on it.

Moreover, we analyze the influence of the incorrected DEM error on the deformation time series estimation. It is worth noting that we do not apply any spatial–temporal filter for the final deformation estimation due to the fact that parameter setting is largely based on operator's experience in real situation. Fig. 9(a)–(c) shows the results of Models 2–4 based on the connected network. Fig. 9(d)–(f) shows the results of these models based on the network with a subset. The results indicate that deformation time series can be affected if DEM error was not well corrected in the MTInSAR models. Among these models, the last model (i.e., Model 4) is most sensitive to the incorrected DEM error when estimating the deformation time series from interferograms having subsets, with a notable decline in mean and STD of RMSE from 1.47/0.38 to 2.04/1.10 mm.

D. Relationship Between DEM Error and Deformation Models

To analyze the relationship between DEM error and deformation models, three deformation models (i.e., linear, periodic, and complicated) are simulated. DEM error, atmospheric signals, and baseline-related noise phase are added. We select a set of connected interferogams with fixed thresholds of spatial and temporal baselines for Models 2–4 and also prepare the single-master observations for Model 1. We then conduct the estimation for these models where only the DEM error and deformation mean rate (or rate vector for Model 4) are taken as parameters no matter linear, periodic, or complicated the simulated "real" deformation is. Fig. 10 shows the results of these models. It is clear that the RMSE

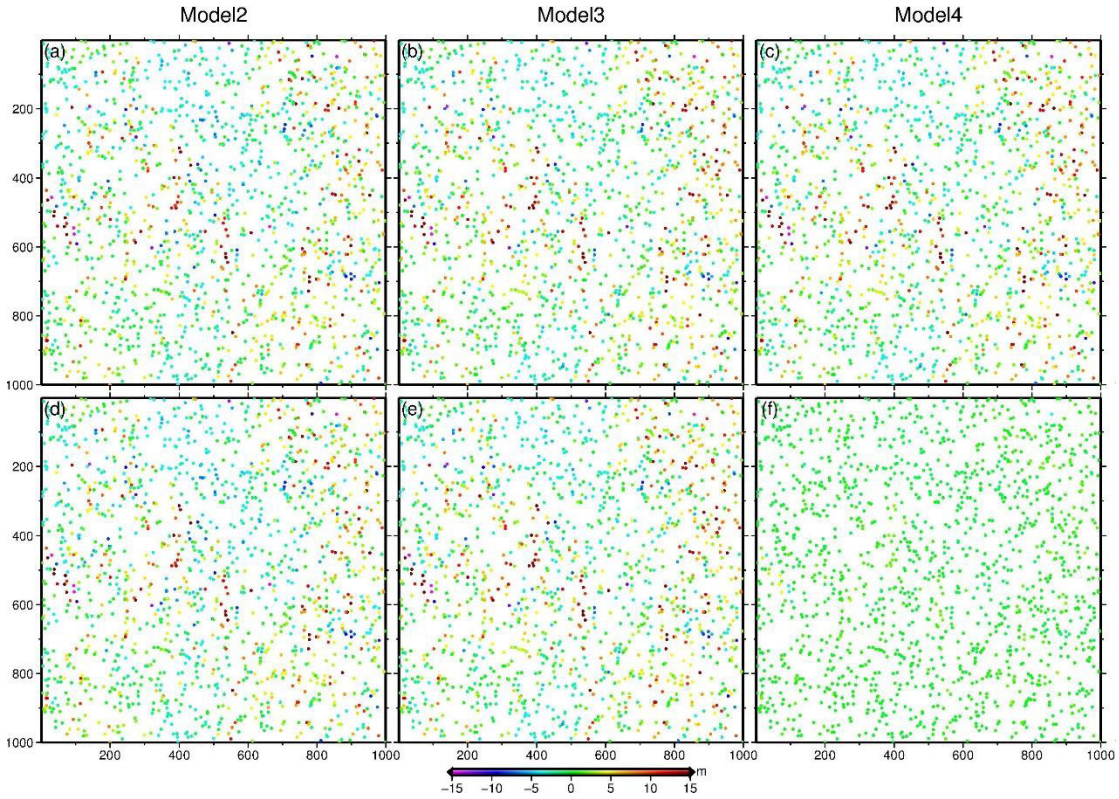

Fig. 7. Estimated DEM errors of Models 2–4 without and with interferogram subset.

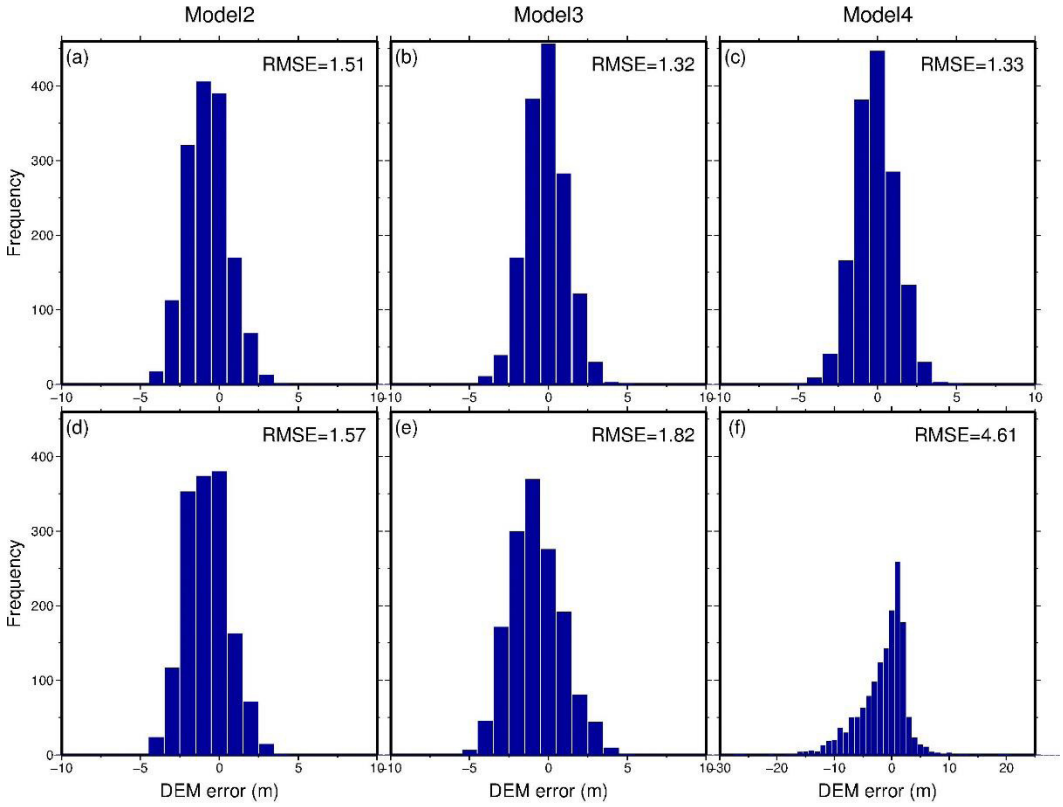

Fig. 8. Histograms of Models 2–4 without and with interferogram subset.

of DEM error estimated by the four models is affected by the discrepancy between the simulated deformation pattern and real deformation signal. For example, the RMSE of DEM error for linear deformation is better than the other two deformation models due to the consistency between the deformation parameter and the real deformation

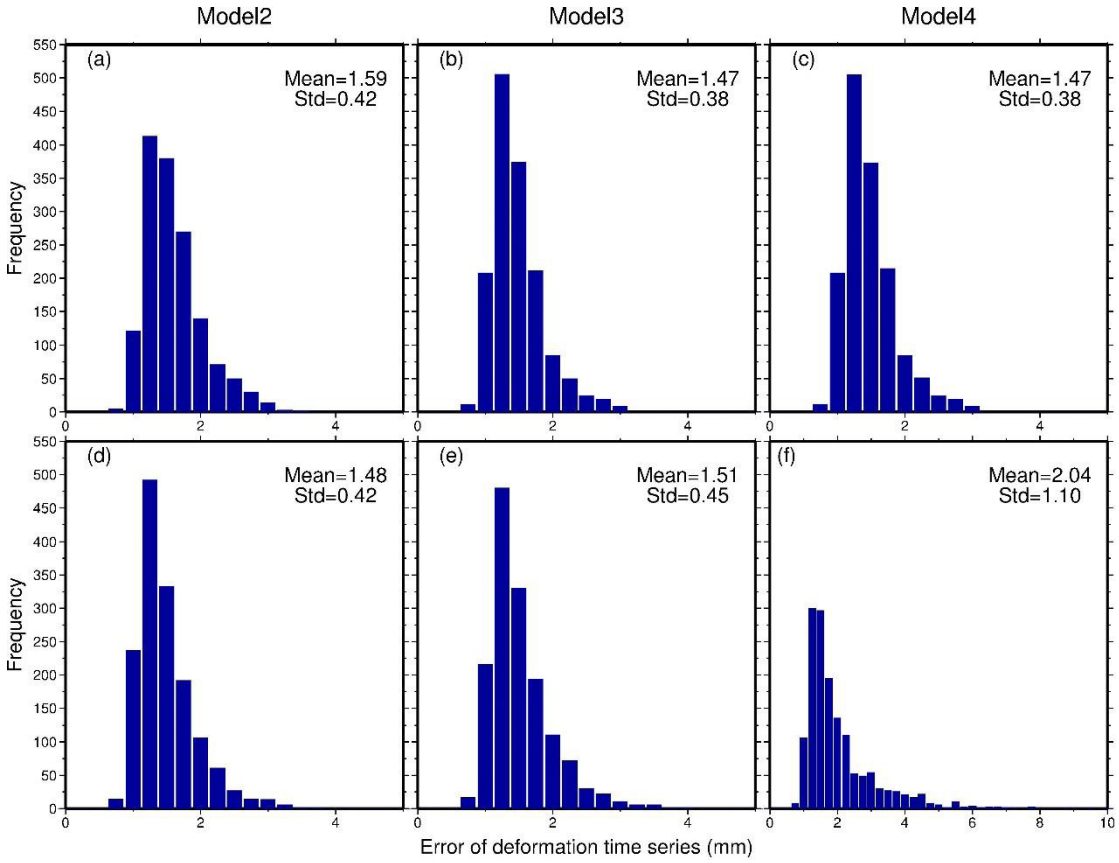

Fig. 9. Histograms of errors of deformation time series estimated by Models 2–4 without and with interferogram subset.

[see Fig. 10(a)–(d)]. The results of Model 2 for the periodic and complicated deformation models are seriously affected by the model bias [see Fig. 10(f) and (j)]. The results of Models 3 and 4 with periodic deformation pattern are similar to the results with linear deformation since signals (i.e., velocities or phases) between adjacent SAR images are taken as parameters in these two models [see Fig. 10(g) and (h)]. However, the RMSE of DEM error estimated by these models with complicated deformation pattern is not satisfactory because the deformation model and real deformation pattern have notable discrepancy [see Fig. 10(j)–(l)]. It is worth noting that accuracy of DEM error estimated by Model 1 (the reference image is January 4, 2009) is also sensitive to the discrepancy between the model used and the real deformation [see Fig. 10(m)]. For example, the RMSE of the estimated DEM error increases from 0.99 m in the linear deformation scenario to 6.93 m in the period scenario, indicating that the proper deformation model is important for DEM error estimation.

For Models 2–4, we also evaluate their performance on DEM error estimation from interferogram stacks with changing baseline thresholds in different deformation scenarios. A set of spatial baseline thresholds changing from 120 to 350 m with an interval of 10 m are used to select image pairs, while the temporal baseline threshold is fixed to a value of 395 days due to its insensitivity to DEM error accuracy described in Section IV-A. The results in Fig. 11(a) show that the RMSE of DEM error of Model 2 is sensitive to the perpendicular baseline thresholds, especially when significant difference existed between deformation model and real deformation, such as period or complicated deformation. Meanwhile, a jump is observed for Models 3 and 4 in Fig. 11(b) and (c) because one SLC image was discarded when using smaller baseline thresholds as depicted in Section IV-B.

As a summary of the synthetic tests, we have studied the estimation of the topographic residuals in MTInSAR, which can affect the DEM reconstruction and the accuracy of the estimated deformation time series based on four widely used models. The factors we have tested here, i.e., the baseline thresholds, the connectivity of interferometric network, the quality of interferograms, and deformation pattern, have been summarized in Table III, which can serve as a reference for MTInSAR model selection. In general, the perpendicular baseline thresholds have an obvious influence on the RMSE of DEM error of Model 2, whereas a slight impact on Models 3 and 4. To the factor of network connectivity, Model 4 is more sensitive compared with Model 3, whereas Model 2 can keep steady in the case having interferogram subset. The RMSE of DEM error of Models 1–4 increases with the increase in atmospheric signals, i.e., the decrease in interferograms' quality. However, Models 3 and 4 in our simulation scenarios are less sensitive to the increasing atmospheric signals compared with Model 2 as shown in Table II. The deformation assumption depicted in Section III-C

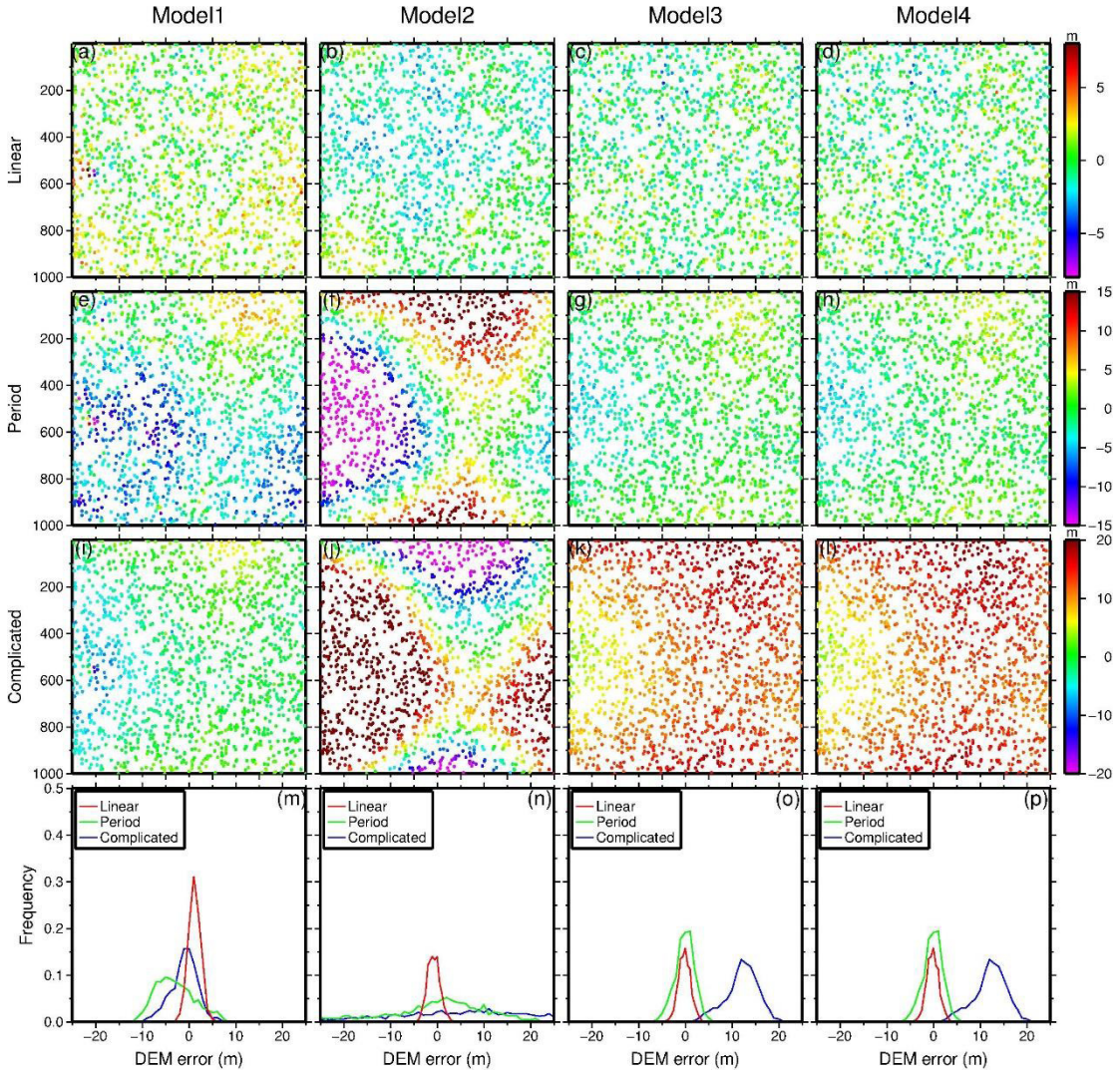

Fig. 10. Estimated DEM errors and histograms of all the four models with three selected deformation patterns. The first three rows represent the estimated DEM error for four models in linear, period, and complicated deformation pattern. The fourth row represents the histograms of estimated DEM error for four models. The red, green, and blue lines represent the statistical results for linear, period, and complicated, respectively.

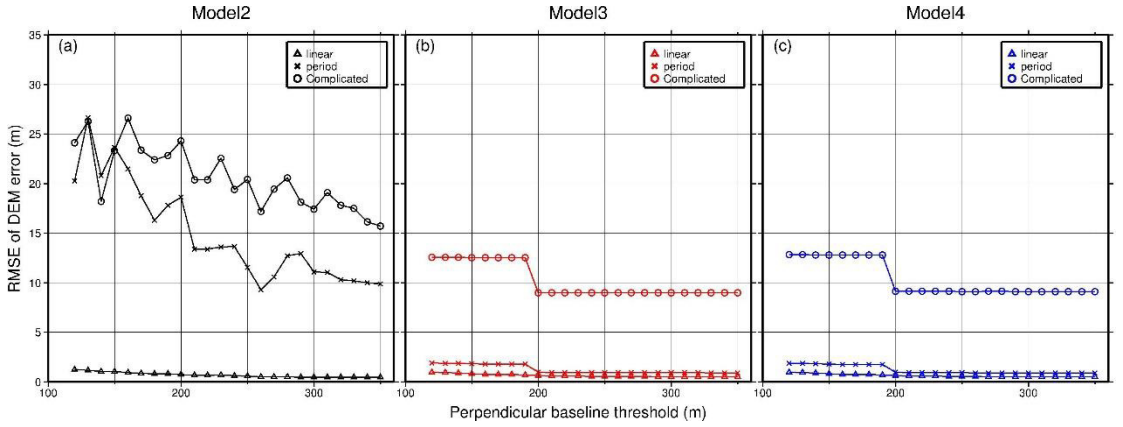

Fig. 11. RMSE of estimated DEM error for three simulated deformation inputs and different baseline thresholds. (a) Model 2. (b) Model 3. (c) Model 4.

has impacts on DEM error estimation for Models 1–4 with different degrees. For example, the influence on Model 2 is most notable, especially when a significant difference existed between assumed deformation model and real deformation, while the stability of other three models is better compared with Model 2.

Although these tests are derived from simulated interferograms based on real SAR data sets and assumptions, for

TABLE III
NOTABILITY OF EFFECTS OF THE AFOREMENTIONED FACTORS ON DEM ERROR ESTIMATION

	Model 1	Model 2	Model 3	Model 4
Baseline thresholds	--	High	Low	Low
Interferogram quality	High	High	High	High
Network connectivity	--	Low	High	High
Deformation assumption	High	High	High	High

example, no phase unwrapping error, zero-Doppler frequency, and no orbit residuals, the conclusions we derived here can largely hold in real cases as the assumptions used can be met by proper processing approaches. It should be underlined that DEM error in interferograms is not only caused by the difference between external DEM and true terrain, which is taken as a parameter in this paper, but the mismatch between the pixel phase centers. Hence, the DEM error estimation especially in high-resolution MTInSAR should take this into consideration.

V. CONCLUSION

By employing vast synthetic tests, this paper has analyzed the accuracy of topographic residuals estimated by MTInSAR techniques, i.e., PSInSAR (Model 1), traditional SBAS (Model 2), Samsnovo's method (Model 3), and Fahatti's method (Model 4). The results indicate that four factors can affect the accuracy of DEM error, and the inaccurately estimated DEM error will further degrade the estimation of deformation time series. The first factor includes the thresholds and the distribution of baselines of image pairs. The RMSE of DEM error is more sensitive to spatial baseline thresholds than temporal baseline threshold, and it is decreased with the increase in perpendicular baseline threshold first and then keeps stable when threshold reaches a certain value. In addition, it also has a strong relationship with the diversity of perpendicular baselines of the selected pairs. The second factor is the quality of differential interferograms. Higher quality (e.g., less atmosphere artifact) can lead to lower RMSE of DEM error. The third one is the connectivity of interferogram network. According to the test, Models 3 and 4 are sensitive to subsets, while Model 2 is stable with the existence of subsets. The last one is the deformation model error. It can result in an inaccurate estimation of DEM error when a significant bias exists in deformation model used and real deformation signal. In the test, the RMSE of the estimated DEM error is notably enlarged when there is a complicated deformation for all the four models.

The work here is expected to raise our awareness of the fact that the quality of topographic residuals retrieved by current MTInSAR techniques can be affected by several factors commonly existing in our real applications. It also provides a guidance on the selection of proper MTInSAR methods. More importantly, by analyzing the factors that can affect the accuracy of retrieved DEM error, it is possible for us to find out an optimal processing framework and modeling strategy to overcome at least partially the limitations associated with current MTInSAR techniques. This is one focus of our work in future.

ACKNOWLEDGMENT

The authors would like to thank the Associate Editor and anonymous reviewers for their constructive comments and suggestions that improved this paper greatly.

REFERENCES

[1] G. C. Feng, X. L. Ding, Z. W. Li, and M. Jiang, "Calibaration of an InSAR-derived coseimic deformation map associated with the 2011 Mw-9.0 Tohoku-Oki earthquake," *IEEE Geosci. Remote Sens. Lett.*, vol. 9, no. 2, pp. 302–306, Mar. 2012.

[2] A. Hooper, H. Zebker, P. Segall, and B. Kampes, "A new method for measuring deformation on volcanoes and other natural terrains using InSAR persistent scatterers," *Geophys. Res. Lett.*, vol. 31, no. 23, art. no. L23611, Dec. 2004.

[3] Q. Sun, L. Zhang, X. L. Ding, J. Hu, Z. W. Li, and J. J. Zhu, "Slope deformation prior to Zhouqu, China landslide from InSAR time series analysis," *Remote Sens. Environ.*, vol. 156, pp. 45–57, Jan. 2015.

[4] P. López-Quiroz, M. P. Doin, F. Tupin, P. Briole, and J.-M. Nicolas, "Time series analysis of Mexico City subsidence constrained by radar interferometry," *J. Appl. Geophys.*, vol. 69, no. 1, pp. 1–15, Sep. 2009.

[5] A. Rucci, D. W. Vasco, and F. Novali, "Monitoring the geologic storage of carbon dioxide using multicomponent SAR interferometry," *Geophys. J. Int.*, vol. 193, no. 1, pp. 197–208, 2013.

[6] M. Costantini *et al.*, "High resolution ground deformations monitoring by COSMO-SkyMed PSP SAR interferometry: Accuracy analysis and validation," presented at the ESA 2011 FRINGE Workshop, Friscati, Italy, Sep. 19–23, 2011.

[7] L. Zhang, Z. Lu, X. Ding, H.-S. Jung, G. C. Feng, and C.-W. Lee, "Mapping ground surface deformation using temporarily coherent point SAR interferometry: Application to Los Angeles Basin," *Remote Sens. Environ.*, vol. 117, pp. 429–439, Feb. 2012.

[8] A. Ferretti, C. Prati, and F. Rocca, "Nonlinear subsidence rate estimation using permanent scatterers in differential SAR interferometry," *IEEE Trans. Geosci, Remote Sens.*, vol. 38, no. 5, pp. 2202–2212, Sep. 2000.

[9] C. Colesanti, A. Ferretti, F. Novali, C. Prati, and F. Rocca, "SAR monitoring of progressive and seasonal ground deformation using the permanent scatterers technique," *IEEE Trans. Geosci. Remote Sens.*, vol. 41, no. 7, pp. 1685–1701, Jul. 2003.

[10] M. Costantini, S. Falco, F. Malvarosa, F. Minati F. Trillo, and F. Vecchioli, "Persistent scatterer pair interferometry: Approach and application to COSMO-SkyMed SAR data," *IEEE J. Sel. Topics Appl. Earth Observ. Remote Sens.*, vol. 7, no. 7, pp. 2869–2879, Jul. 2014.

[11] M. Costantini, F. Minati, F. Trillo, and F. Vecchioli, "Enhanced PSP SAR interferometry for analysis of weak scatterers and high definition monitoring of deformations over structures and natural terrains," in *Proc. IEEE Int. Geosci. Remote Sens. Symp. (IGARSS)*, Jul. 2013, pp. 876–879.

[12] L. Zhang, X. Ding, and Z. Lu, "Modeling PSInSAR time series without phase unwrapping," *IEEE Trans. Geosci. Remote Sens.*, vol. 49, no. 1, pp. 547–556, Jan. 2011.

[13] P. Berardino, G. Fornaro, R. Lanari, and E. Sansosti, "A new algorithm for surface deformation monitoring based on small baseline differential SAR interferograms," *IEEE Trans. Geosci. Remote Sens.*, vol. 40, no. 11, pp. 2375–2383, Nov. 2002.

[14] M.-P. Doin *et al.*, "Presentation of the small baseline NSBAS processing chain on a case example: The Etna deformation monitoring from 2003 to 2010 using Envisat data," presented at the ESA 2011 FRINGE Workshop, Friscati, Italy, Sep. 19–23, 2011.

[15] O. Mora, J. J. Mallorqui, and A. Broquetas, "Linear and nonlinear terrain deformation maps from a reduced set of interferometric SAR images," *IEEE Trans. Geosci. Remote Sens.*, vol. 41, no. 10, pp. 2243–2253, Oct. 2003.

[16] G. Ducret, M.-P. Doin, R. Grandin, C. Lasserre, and S. Guillaso, "DEM corrections before unwrapping in a small baseline strategy for InSAR time series analysis," *IEEE Trans. Geosci. Remote Sens. Lett.*, vol. 11, no. 3, pp. 696–700, Mar. 2014.

[17] C. Y. Zhao, Z. Lu, Q. Zhang, and J. de la Fuente, "Large-area landslide detection and monitoring with ALOS/PALSAR imagery data over Northern California and Southern Oregon, USA," *Remote Sens. Environ.*, vol. 124, pp. 348–359, Sep. 2012.

[18] S. Samsonov, M. van der Kooij, and K. Tiampo, "A simultaneous inversion for deformation rates and topographic errors of DInSAR data utilizing linear least square inversion technique," *Comput. Geosci.*, vol. 37, no. 8, pp. 1083–1091, Aug. 2011.
[19] S. Samsonov, "Topographic correction for ALOS PALSAR interferometry," *IEEE Trans. Geosci, Remote Sens.*, vol. 48, no. 7, pp. 3020–3027, Jul. 2010.
[20] H. Fattahi and F. Amelung, "DEM error correction in InSAR time series," *IEEE Trans. Geosci. Remote Sens.*, vol. 51, no. 7, pp. 4249–4259, Jul. 2013.
[21] Y. H. Zhang, H. A. Wu, and G. T. Sun, "Deformation model of time series interferometric SAR techniques," *Acta Geodaetica Cartograph. Sin.*, vol. 41, no. 6, pp. 864–869, Dec. 2012.
[22] A. Ferretti, C. Prati, and F. Rocca, "Permanent scatterers in SAR interferometry," *IEEE Trans. Geosci. Remote Sens.*, vol. 39, no. 1, pp. 8–20, Jan. 2001.
[23] F. Rocca, "Diameters of the orbital tubes in long-term interferometric SAR surveys," *IEEE Trans. Geosci. Remote Sens. Lett.*, vol. 1, no. 3, pp. 224–227, Jul. 2004.
[24] F. Casu, M. Manzo, A. Pepe, and R. Lanari, "SBAS-DInSAR analysis of very extended areas: First results on a 60 000-km^2 test site," *IEEE Trans. Geosci. Remote Sens.*, vol. 5, no. 3, pp. 438–442, Jul. 2008.
[25] A. N. Tikhonov, *Solution of Ill-Posed Problem*. New York, NY, USA: Wiley, 1977.
[26] Q. Q. Wang, R. Hu, and P. Blonigan, "Least squares shadowing sensitivity analysis of chaotic limit cycle oscillations.," *J. Comput. Phys.*, vol. 267, pp. 210–224, Jun. 2014.
[27] P. Tizzani *et al.*, "Surface deformation of Long Valley Caldera and Mono Basin, California, investigated with the SBAS-InSAR approach," *Remote Sens. Environ.*, vol. 108, no. 3, pp. 277–289, Jun. 2007.
[28] B. M. Kampes, *Radar Interferometry*. Dordrecht, The Netherlands: Springer, 2006.
[29] R. F. Hanssen, *Radar Interferometry: Data Interpretation and Error Analysis*. Dordrecht, The Netherlands: Kluwer, 2001.
[30] H. A. Zebker and J. Villasenor, "Decorrelation in interferometric radar echoes," *IEEE Trans. Geosci. Remote Sens.*, vol. 30, no. 5, pp. 950–959, Sep. 1992.
[31] L. Zhang, X. Ding, Z. Lu, H.-S. Jung, J. Hu, and G. C. Feng, "A novel multitemporal InSAR model for joint estimation of deformation rates and orbital errors," *IEEE Trans. Geosci Remote Sens.*, vol. 56, no. 6, pp. 3529–3540, Jun. 2014.

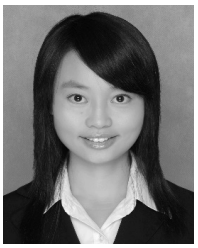

Yanan Du received the B.S. degree from the School of Geosciences and Info-Physics, Central South University, Changsha, China, in 2011, where she is currently pursuing the Ph.D. degree in geodesy and survey engineering.

Her current research interests include interferometric synthetic aperture radar and its applications on digital elevation model reconstruction and surface deformation mapping.

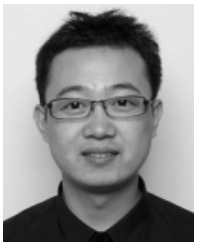

Lei Zhang (S'08–M'11) was born in Yantai, China, in 1981. He received the M.Sc. degree from Tongji University, Shanghai, China, in 2007, with a thesis on fault slip inversion with interferometric synthetic aperture radar (SAR) and GPS data based on a triangular dislocation model, and the Ph.D. degree in geodesy and geodynamics from The Hong Kong Polytechnic University, Hong Kong, in 2011.

Since 2012, he has been a Research Assistant Professor with the Department of Land Surveying and Geo-Informatics, The Hong Kong Polytechnic University. His current research interests include developing advanced processing techniques for SAR data and the application of multitemporal interferometric analysis on the retrieval of ground displacement and geophysical parameters, with an emphasis on natural hazard monitoring and mitigation.

Guangcai Feng received the master's degree in surveying engineering from Central South University, Changsha, China, in 2006, and the Ph.D. degree in geophysics and geodesy from The Hong Kong Polytechnic University, Hong Kong, in 2011.

He is currently an Associate Professor with the Department of Surveying and Remote Sensing, School of Geoscience and Info-Physics, Central South University. His research interests include interferometric synthetic aperture radar for inverting source parameters of earthquakes and ground deformation monitoring in urban areas.

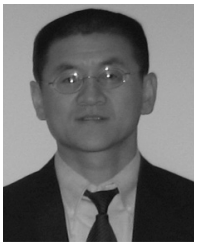

Zhong Lu received the B.S. and M.S. degrees from Peking University, Beijing, China, in 1989 and 1992, respectively, and the Ph.D. degree from the University of Alaska Fairbanks, Fairbanks, AK, USA, in 1996.

He was a Physical Scientist with the U.S. Geological Survey (USGS) from 1997 to 2013, and is currently a Professor and Endowed Shuler-Foscue Chair with the Huffington Department of Earth Sciences, Southern Methodist University, Dallas, TX, USA. He is also a Principal Investigator of projects funded by NASA, ESA, JAXA, DLR, and USGS on the study of land surface deformation using satellite interferometric synthetic aperture radar (InSAR) imagery. He has authored more than 45 and coauthored 90 peer-reviewed journal articles and book chapters focused on InSAR techniques and applications. His new book is *InSAR Imaging of Aleutian Volcanoes: Monitoring a Volcanic Arc from Space* (Springer, 2014). His current research interests include technique developments of synthetic aperture radar, InSAR, and persistent scatterer InSAR processing and their applications on natural hazard monitoring and natural resource characterization.

Dr. Lu is a Committee Member of the International User Team for Radarsat-C SAR Constellations, the GeoEarthscope InSAR User Working Group, NASA's Alaska Satellite Facility User Working Group, and the upcoming NASA-India SAR Science Definition Team. He is also a member of the editorial boards of the *International Journal of Image and Data Fusion, Geomatics, Natural Hazards and Risk, and Dataset Papers in Geosciences*. He was a recipient of the American Society for Photogrammetry and Remote Sensing Award for Best Scientific Paper in *Remote Sensing*, NASA Group Achievement Award, NASA Certificate of Appreciation, Raytheon Distinguished Level Award for Excellence in Technology, Science Applications, International Corporation Technical Fellow, and Jerald Cook Memorial Award. He is the Chair of the Western North America InSAR Consortium. He is an Associate Editor of *Remote Sensing and Frontier in Volcanology*.

Qian Sun was born in Suqian, China, in 1983. She received the master's and Ph.D. degrees in geodesy and surveying engineering from Central South University, Changsha, China, in 2009 and 2015, respectively.

She is currently a Lecturer with the College of Resources and Enviromental Science, Hunan Normal University, Changsha. Her research interests include monitoring geohazards with multitemporal interferometric satellite synthetic aperture radar.